Retrieval of cloud fraction and optical thickness from multi-angle polarization observations

Claudia Emde[1,2], Veronika Pörtge[1], Mihail Manev[1], and Bernhard Mayer[1]

[1]Meteorologisches Institut, Ludwig-Maximilians-Universität München, Germany
[2]Institut für Physik der Atmosphäre, Deutsches Zentrum für Luft- und Raumfahrt (DLR), Germany

Correspondence: Claudia Emde (claudia.emde@lmu.de)

Abstract. We introduce an innovative method to retrieve cloud fraction and optical thickness based on polarimetry. The approach is well-suited for satellite observations providing multi-angle polarization measurements, such as the Hyper-Angular Rainbow Polarimeter (HARP2), the Spectro-Polarimeter for Planetary EXploration (SPEX), and the Multi-viewing Multi-channel Multi-polarisation Imager (3MI). The cloud fraction and the cloud optical thickness can be derived for each pixel from measurements at two viewing angles: one within the cloudbow at a scattering angle of approximately 140° and a second in the sun-glint region or at a scattering angle of approximately 90°. In the cloudbow, the degree of polarization depends mainly on the cloud optical thickness. Conversely, for a viewing direction in the sun-glint region or around 90° scattering angle, the degree of polarization depends on the clear fraction of the pixel, because at these scattering angles radiation scattered by cloud droplets is almost unpolarized whereas radiation reflected by the surface or scattered by molecules is highly polarized. Utilizing these dependencies, we developed a straightforward retrieval algorithm using a lookup-table approach.

As a demonstration, we apply the methodology to airborne observations from polarization cameras of the Munich Aerosol Cloud Scanner (specMACS) instrument. The high spatial resolution data (10-20 m) has been averaged to a spatial resolution of approximately 2.5 km to mimic satellite observations. A comparison of the derived cloud fractions with the high spatial resolution images for specific cases, featuring low, medium and high cloud fractions, demonstrates the expected performance of the retrieval.

1 Introduction

Clouds influence local weather conditions as well as the Earth's climate system. They affect the energy balance and play a large role in the planet's long-term climate. According to the latest IPCC assessment report AR6 (Intergovernmental Panel On Climate Change, 2023), there have been major advances in the understanding of cloud processes over the last decade that have decreased the uncertainty range for the cloud feedback by about 50% compared to AR5 (Intergovernmental Panel On Climate Change, 2014) but nevertheless, clouds remain the largest contribution to the overall uncertainty in climate feedbacks.

In order to further improve the representation of clouds in climate models more observations are required. Important quanti-
ties to characterize the interaction of radiation with cloud droplets or particles are the cloud phase, the cloud optical thickness,
25   the cloud fraction, and the droplet or particle size distribution.

A commonly used method to derive the cloud optical thickness and effective droplet size in the solar spectral region is
based on observations at two wavelengths, a non-absorbing one in the visible wavelength range which is mainly sensitive to
cloud optical thickness, and an absorbing one in the near infrared which also depends on the droplet size (Nakajima and King,
1990). This methodology is included in operational satellite retrieval algorithms (e.g. for the Moderate Resolution Imaging
30   Spectroradiometer MODIS, Platnick et al., 2017). MODIS has a relatively high spatial resolution of about 1×1 km^2. Among
the MODIS cloud products is also the cloud fraction which is retrieved on a spatial resolution of 5×5 km^2 by computing the
ratio of pixels where clouds have been detected and the clear pixels for this larger region including 25 individual MODIS pixels
(Platnick et al., 2017).

In order to simultaneously retrieve droplet size, and information on the width of the droplet size distribution polarimetric
35   observations of the cloudbow have been applied. This method was first used to determine the microphysical properties of the
sulfuric acid clouds on Venus (Hansen and Hovenier, 1974). For Earth, it has been used to derive liquid water cloud droplet
size distributions from satellite observations using the POLarization and Directionality of the Earth's Reflectances (POLDER)
instrument (Bréon and Doutriaux-Boucher, 2005) and from airborne observations with high spatial resolution (Alexandrov
et al., 2012; Pörtge et al., 2023). Similar to Venus, average liquid cloud properties have been retrieved for Earth via Earthshine
40   observations (Sterzik et al., 2020).

The aerosol retrieval algorithm based on an optimal estimation approach developed by Hasekamp (2010) derives, in addition
to aerosol optical properties, also the cloud fraction from POLDER measurements with a spatial resolution of about 7×6 km^2.
In a validation study for partially cloudy scenes based on simulated data by Stap et al. (2016a, b) it has been shown that
the retrieved cloud fraction correlates well with the cloud fraction used as input for radiative transfer simulations to produce
45   the simulated data. Van Diedenhoven et al. (2007) developed a retrieval method for cloud parameters from satellite-based
reflectance measurements (Global Ozone Monitoring Experiment (GOME) and Scanning Imaging Absorption Spectrometer
for Atmospheric Chartography (SCIAMACHY)) in the ultraviolet and the oxygen A-band. Based on an optimal estimation
approach they derive cloud fraction, cloud optical thickness, and cloud top pressure. The oxygen-A band contains information
about cloud optical thickness and cloud top pressure. The UV spectral region is also sensitive to cloud fraction, since the
50   Rayleigh scattering contribution to the reflectance increases with the clear fraction of the pixel.

The NASA Plankton, Aerosol, Cloud, ocean Ecosystem (PACE) mission (https://pace.oceansciences.org) which has suc-
cessfully been launched on 8th of February 2024 includes two polarimeters, the Spectro-polarimeter for Planetary Exploration
(SPEXone) and the Hyper Angular Research Polarimeter (HARP2) (Remer et al., 2019). SPEXone provides hyper-spectral po-
larized radiances in the spectral range from 385–770 nm in five viewing directions for a narrow swath of 100 km at nadir. The
55   spatial resolution is about 5 km and global coverage is obtained after approximately 30 days. HARP2 is a hyper-angular instru-
ment, with four spectral bands between 440 nm and 870 nm and observes a wide swath of 1555 km at nadir. For the 669 nm

band HARP2 includes 60 viewing angles spaced over 114°. The spatial resolution is approximately the same as SPEXOne. Due to the wider swath global coverage can be obtained in two days.

The Multi-Viewing Multi-Channel Multi-Polarisation Imaging (3MI) instrument is an optical radiometer dedicated primarily
60   to aerosol characterization (Fougnie et al., 2018). It is one of the missions of the EUMETSAT Polar System Second Generation (EPS-SG) program planned to be launched in 2025. It will provide a multi-spectral (from 410 to 2130 nm), multi-polarisation (-60°, 0°, and +60°), and multi-angular (14 views) image of the outgoing radiance at the top of the atmosphere. The spatial resolution is 4 km at nadir and the swath width is 2200 km. A secondary mission objective is to improve the cloud characterisation, in particular cloud phase, cloud microphysics (phase and effective particle size), cloud height, and cloud optical
65   thickness.

In this paper we present a novel method to retrieve the cloud optical thickness along with the cloud fraction, which could be a valuable addition to operational cloud retrieval algorithms for upcoming satellite instruments providing multi-angle polarization observations. The retrieval method requires the degree of linear polarization at two angles, one in the cloudbow region which is sensitive to cloud optical thickness and another angle, preferably at a scattering angle around 90° which is mainly sen-
70   sitive to the cloud fraction. Such observations will be available from HARP2, SPEXOne and 3MI. Our method performs best over ocean, because of the high polarization of the sun-glint, which causes a clear correlation between degree of polarization and the cloud fraction.

The paper is structured as follows: In Section 2 the dependence of the degree of polarization on cloud optical thickness and cloud fraction is investigated and retrieval lookup tables for different atmosphere and surface conditions are constructed to
75   show how cloud fraction and cloud optical thickness can be retrieved. In Section 3 we apply the retrieval method on airborne observations of the specMACS instrument and present the results. The final Section 4 includes a summary, discusses limitations and provides an outlook on future work.

2   Methodology

2.1   General setup

80   For all simulations we used the Monte Carlo radiative transfer model MYSTIC (Mayer, 2009; Emde et al., 2010) implemented in the libRadtran package (Mayer and Kylling, 2005; Emde et al., 2016). MYSTIC is a comprehensive vector radiative transfer model that can be run in 1D or 3D, plane-parallel or spherical geometry. For this study we applied the freely available 1D plane-parallel version that has been extensively validated in various model intercomparison studies (e.g., Emde et al., 2015).

The general setup for all simulations is as follows: we take the US-standard atmosphere from Anderson et al. (1986) to set up
85   the profiles of pressure, temperature, and trace gas concentrations. As incoming solar irradiance we use the simulated spectrum by Kurucz and Bell (1995). We enable the polarisation mode (Emde et al., 2010) to compute the complete Stokes vector, and the variance reduction methods (Buras and Mayer, 2011) for accurate simulations including cloud scattering. We perform monochromatic simulations at 667 nm, approximately the center wavelength of the HARP2 instrument. The solar zenith angle is set to 50°. The simulations are performed for viewing angles from -60° to +60° in steps of 1° in the solar principal plane,

thus we obtain the Stokes vector for scattering angles Θ from 70° to 180°. The scattering angle is defined as the angle between the sun position vector (incident direction) and viewing direction vector (i.e., the sun is behind the observer at 180°). As we will show later, the retrieval performs best for observations in the solar principal plane including the maximum of the sun-glint.

All simulations are performed for a clear sky atmosphere and for a liquid cloud layer located from 2–3 km, respectively. The optical thickness of the cloud is varied between 1 and 50. Cloud droplet sizes are gamma distributed with an effective radius of 10 μm and an effective variance of 0.1. Cloud optical properties were calculated using the Mie program included in libRadtran (Mie, 1908; Wiscombe, 1980).

The components of Stokes vector $\mathbf{I}$ are defined as time averages of linear combinations of the electromagnetic field vector (Chandrasekhar, 1950; Hansen and Travis, 1974):

$$I = \left\langle E_\parallel E_\parallel^* + E_\perp E_\perp^* \right\rangle, \tag{1}$$

$$Q = \left\langle E_\parallel E_\parallel^* - E_\perp E_\perp^* \right\rangle, \tag{2}$$

$$U = \left\langle E_\parallel E_\perp^* + E_\perp E_\parallel^* \right\rangle, \tag{3}$$

$$V = i \left\langle E_\parallel E_\perp^* - E_\perp E_\parallel^* \right\rangle. \tag{4}$$

Here, $E_\parallel$ and $E_\perp$ are the components of the electric field vector parallel and perpendicular to the reference plane, respectively. I is the intensity of the radiation, Q and U give the state of linear polarization and V the circular polarization. The unit of the Stokes components is $\mathrm{W/(m^2\ nm\ sr)}$. We will neglect V in the following because circular polarization is several orders of magnitude smaller than linear polarization (e.g., Emde et al., 2018). In the solar principal plane, U is exactly 0 for a model consisting of homogeneous layers by definition. Therefore the signed degree of linear polarization is given by

$$P = Q/I \tag{5}$$

A negative (positive) P means that the radiation is predominantly polarized perpendicular (parallel) to the scattering plane. Note that P is a dimensionless quantity which can be measured without absolute calibration. In the following, we call the directional dependence of radiance on the scattering angle $\mathbf{I}(\Theta)$ the "phase curve" and the directional dependence of the degree of polarization $P(\Theta)$ the "polarized phase curve".

In order calculate the Stokes vector for a partially cloudy pixel we combine the clear and the cloudy simulations, which is commonly called independent pixel approximation (IPA):

$$\mathbf{I} = (1-c) \cdot \mathbf{I}_{\mathrm{clear}} + c \cdot \mathbf{I}_{\mathrm{cloudy}} \tag{6}$$

Here c is the cloud fraction of the pixel, $\mathbf{I}_{\mathrm{clear}}$ is the Stokes vector simulated for clear sky, and $\mathbf{I}_{\mathrm{cloudy}}$ is the Stokes vector simulated for the cloudy sky. The degree of linear polarization of a partially cloudy pixel is

$$P = \frac{(1-c)Q_{\mathrm{clear}} + cQ_{\mathrm{cloudy}}}{(1-c)I_{\mathrm{clear}} + cI_{\mathrm{cloudy}}} \tag{7}$$

Note that it can not be calculated as the linear combination of the individual degrees of polarization.

 ## 2.2   Retrieval of cloud optical thickness and cloud cover from degree of polarization

In this section we analyze the sensitivity of the polarized phase curve on cloud fraction and cloud optical thickness. In addition, we investigate the impact of wind speed, aerosols and cloud altitude.

2.2.1   Sensitivity and retrieval lookup tables for ocean surface
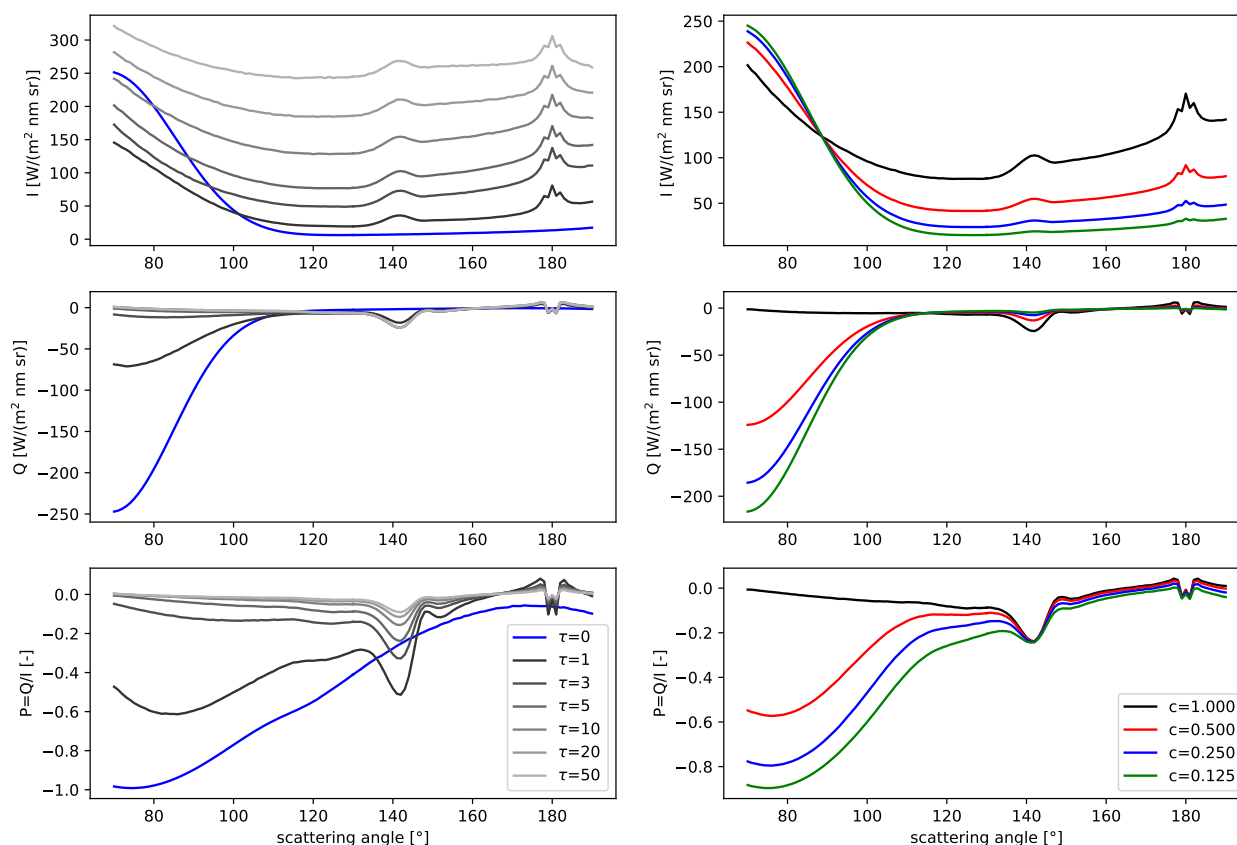
Figure 1. *Left:* Sensitivity of phase curve on cloud optical thickness τ at 667 nm. *Right:* Phase curve for fixed $\tau = 5$ for various cloud fractions. All simulations are for an ocean surface, a wind speed of 5 m/s and a solar zenith angle of 50°. Cloud droplets sizes are modeled using a gamma distribution with an effective radius of 10 μm and an effective variance of 0.1.

In the following, we include an ocean surface which is modelled using the reflectance matrix based on the Fresnel equations
 convolved with a Gaussian kernel to account for the ocean waves (Mishchenko and Travis, 1997; Tsang et al., 1985; Cox and Munk, 1954a, b). Water surface reflection causes very strong polarization in the sun-glint. The wind speed which determines the spread of the sun-glint region is set to 5 m/s. Results of those simulations are shown in the left panel of Figure 1. The blue line corresponds to the clear sky simulation. The top panel shows the total intensity I, the middle panel the linearly polarized

intensity which is equal to the Q-component of the Stokes vector in the solar principal plane, and the bottom panel is the degree
of linear polarization Q/I. The U-component of the Stokes vector is zero in the principal plane. The figures clearly show the
broad sun-glint region at scattering angles around $100°$. The degree of linear polarization of the sun-glint is close to 1 for clear
sky (see blue line in lower left panel). The Q-component (middle left panel) is negative which means that the polarization
direction is perpendicular to the scattering plane.

The grey lines in the left panels correspond to various cloud optical thicknesses from 1 (dark grey) to 50 (light grey).
The intensity (unpolarized radiance I) increases with increasing cloud optical thickness since more radiation is reflected. The
linearly polarized radiance Q saturates relatively quickly around $\tau = 5$. All curves show two distinct features, the cloudbow at
scattering angles around $140°$ and the backscatter glory around $180°$. In particular the cloudbow is highly polarized. Looking
at the Q-results we find that the linear polarization predominantly emerges from surface reflection at scattering angles around
$80°$ and mainly from cloud scattering at scattering angles around $140°$.

We then calculate the Stokes vector for a fixed cloud optical thickness of 5 for cloud fractions between 1/8 and 1 (fully
cloudy), the results are shown in the right panels of Fig. 1. The black line corresponds to full cloud cover (c=1) and is identical
to the line for τ=5 in the left panels. When we focus on the degree of linear polarization Q/I we see, that it does not depend
on cloud fraction in the cloudbow region, whereas there is a strong dependence on cloud fraction in the glint region. The
reason is that surface reflection and Rayleigh scattering begin to contribute to the degree of linear polarization significantly
only at angles smaller than about $110°$. For partly cloudy pixels a part of the surface is seen by the observer, and therefore, the
degree of polarization is increased in glint directions. In the cloudbow region, only the cloud contributes to the degree of linear
polarization, therefore the degree of linear polarization is not changed when a part of the surface becomes visible.
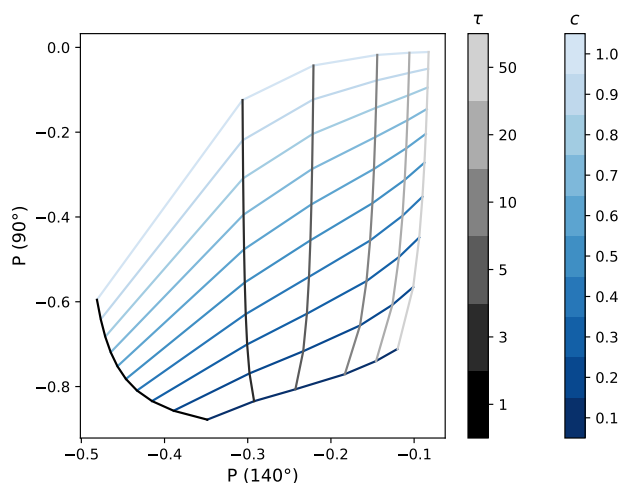
Figure 2. Lookup table for cloud cover and cloud optical thickness retrieval. The blue lines correspond to constant cloud fractions and the
grey lines correspond to constant cloud optical thickness values.

Using these dependencies allows us to generate a retrieval lookup table as illustrated in Figure 2. Here we plotted the degree of polarization at Θ=140° ($P(140°)$) on the x-axis and the degree of polarization at Θ=90° ($P(90°)$) on the y-axis. The blue lines correspond to constant cloud fraction values, i.e. the upper light blue line is for a cloud fraction of 1.0 (fully cloudy) and the lower dark blue line is for a cloud fraction of 0.1. The grey lines correspond to constant cloud optical thickness values between 1 (dark grey) and 50 (light grey). The lookup-table plot illustrates, that cloud fraction and cloud optical thickness can be retrieved from the degree of linear polarization observed at the two viewing angles since the blue and grey lines separate nicely.

2.2.2 Sensitivity over a dark land surface
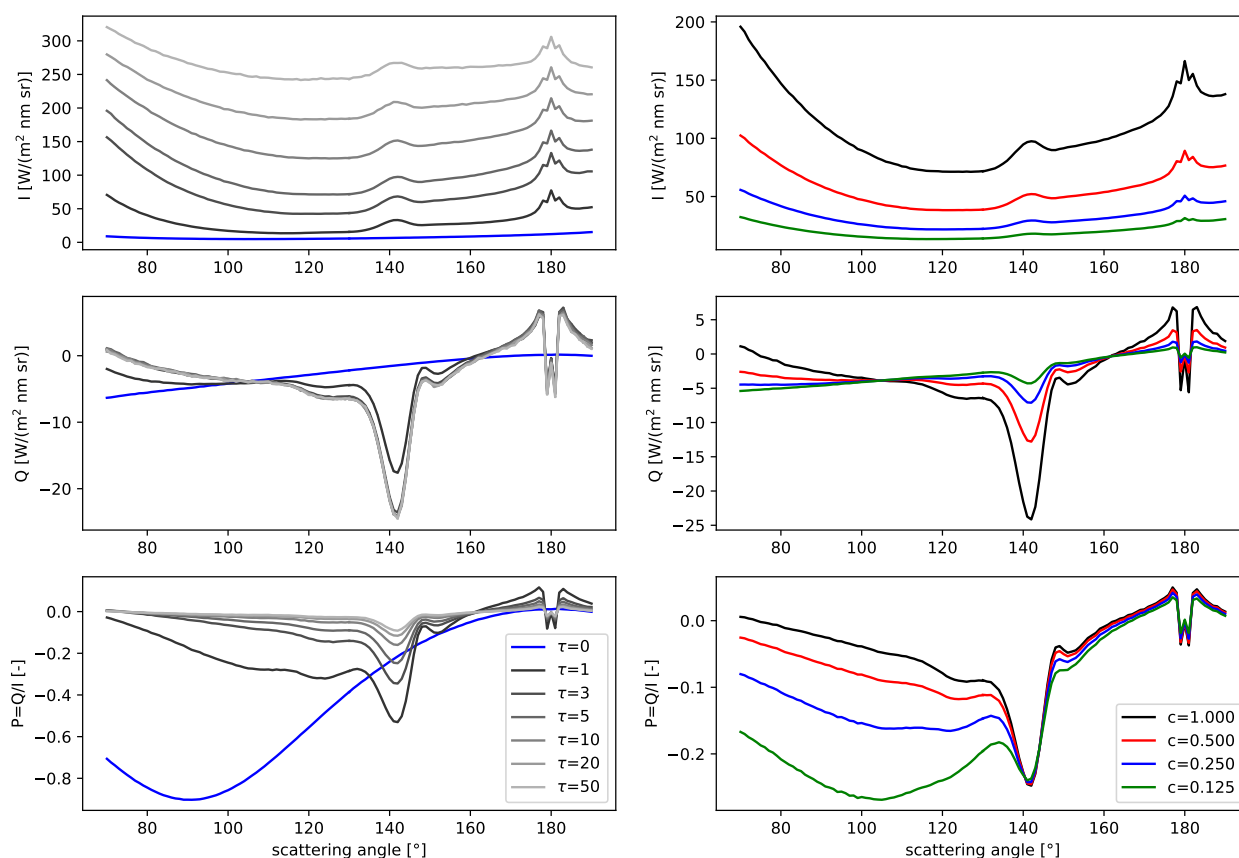
Figure 3. *Left:* Sensitivity of phase curve on cloud optical thickness τ at 667 nm. *Right:* Phase curve for fixed $\tau = 5$ for various cloud fractions. All simulations are for a dark land surface (Lambertian surface with albedo=0.0) and a solar zenith angle of 50°. Cloud droplets sizes are modeled using a gamma distribution with an effective radius of 10 μm and an effective variance of 0.1.

In this Section we present the same simulations as in the previous Section 2.2.1 but for a dark land surface instead of an ocean surface. The results are shown in Fig. 3. The left panels show 1D plane parallel simulations including a cloud layer with varying

optical thickness as grey lines and the clear sky simulation in blue. As expected there is no sun-glint, but nevertheless, the blue line shows a high degree of polarization with a maximum at a scattering angle of 90° due to Rayleigh scattering. However, the magnitudes of I and Q are both small for clear sky because the molecular atmosphere reflects much less radiation than the cloud layer or an ocean surface in the sun-glint region. When we now combine the simulations for clear sky and cloudy sky according to the IPA approximation (Eqs. 6,7) we find that the results are dominated by the cloud layer, even at scattering angles around 90° (right panels of Fig. 3). Therefore the degree of polarization for partially cloudy pixels over a dark land surface is much smaller for viewing angles around 90° than for the ocean surface with the very bright and strongly polarizing sun-glint. Still we find a good separation of P at scattering angles around 90° for the various cloud fractions.

2.2.3 Retrieval lookup tables for various scenarios

Fig. 4 shows polarized phase curves and the corresponding lookup tables for various scenarios. The upper row (a) corresponds to the scenario presented in the previous section, with an ocean surface and a wind speed of 5 m/s.

To investigate the influence of wind speed on the polarized phase curve, we conducted identical simulations with a wind speed of 10 m/s (scenario (b)). We find that the maximum degree of polarization for partially cloudy pixels is decreased and also the slope of P is smaller between 90° and 110° scattering angle. The lookup table generated for higher wind speeds looks similar to that of the previous case and is just as good to retrieve optical thickness and cloud fraction.

The presence of aerosols also modifies the polarization state. Therefore, we repeated the simulations with additional aerosols corresponding to the mixture "maritime clean" as defined in the OPAC database (Hess et al., 1998; Emde et al., 2016) with an aerosol optical thickness set to 0.1 (scenario (c)). Compared to the results without aerosols, we find that the degree of polarization is slightly decreased due to increased multiple scattering, as expected. Furthermore, the polarized phase curves closely follow the same pattern as the scenario (a) and also the lookup table appears nearly identical.

Finally, we test whether the methodology would also work for land surfaces. We use a Lambertian surface as an approximation which depolarizes the reflected light completely. This is a realistic approximation as the largest polarized reflectances[1] observed by the PARASOL instrument over land are in the range between 0.02 and 0.04 (Maignan et al., 2009). Row (d) of Fig. 4 shows the simulations for a dark surface (albedo=0.0, scenario (d)). The blue line in the left figure shows the simulation for clear sky and we see the high degree of polarization around 90° scattering angle. When a cloud is added, the degree of polarization is smaller than for the corresponding cases over ocean, because the polarized reflectance from Rayleigh scattering is much smaller than from reflection in the sun-glint (see also Fig. 3). The lookup-table plot indicates that, for small cloud optical thicknesses and low cloud fractions, the lines are distinct, but as the cloud optical thickness increases, the lines converge. This convergence may lead to less accurate retrieval results for the same measurement accuracy. If the surface albedo is nonzero, this situation becomes worse. Row (e) of Fig. 4 shows the results for a surface albedo of 0.2. In this case the surface depolarizes and the entire lookup-table is compressed making a retrieval impossible.

---

[1]In the solar principal plane the polarized reflectance is defined as $R_p = \frac{\pi Q}{E_0 \cos\theta_0}$, where E_0 is the extraterrestrial solar irradiance and θ_0 is the solar zenith angle.
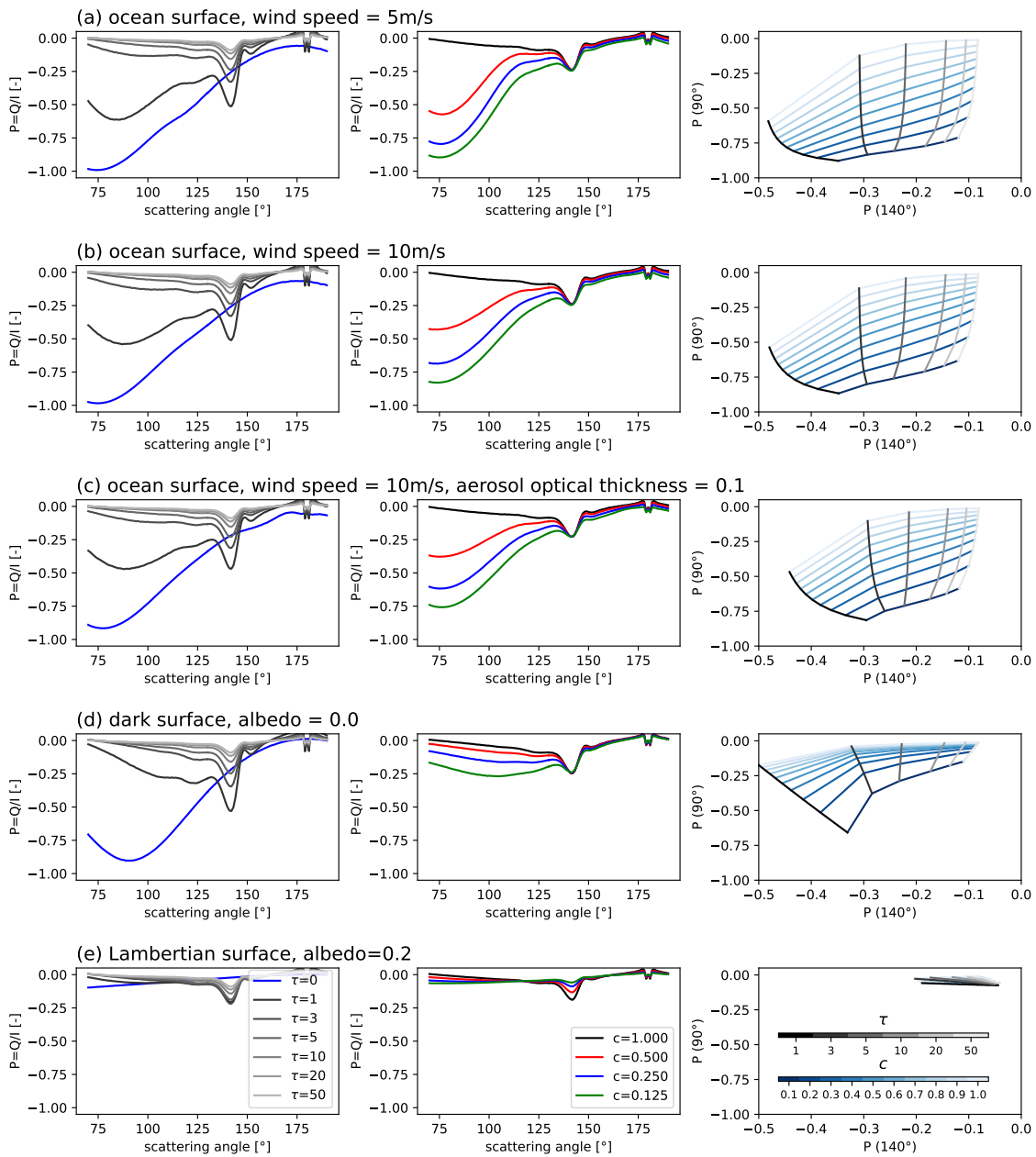
Figure 4. Polarized phase curves and retrieval lookup tables for various scenarios. The left figures show simulations for a homogeneous cloud layer and the grey lines correspond to different cloud optical thicknesses. The blue lines correspond to the clear sky simulation. The middle plots show the polarized phase curves for partially cloudy pixels. The right panels show the corresponding retrieval lookup tables, the line colors correspond to Fig.2.
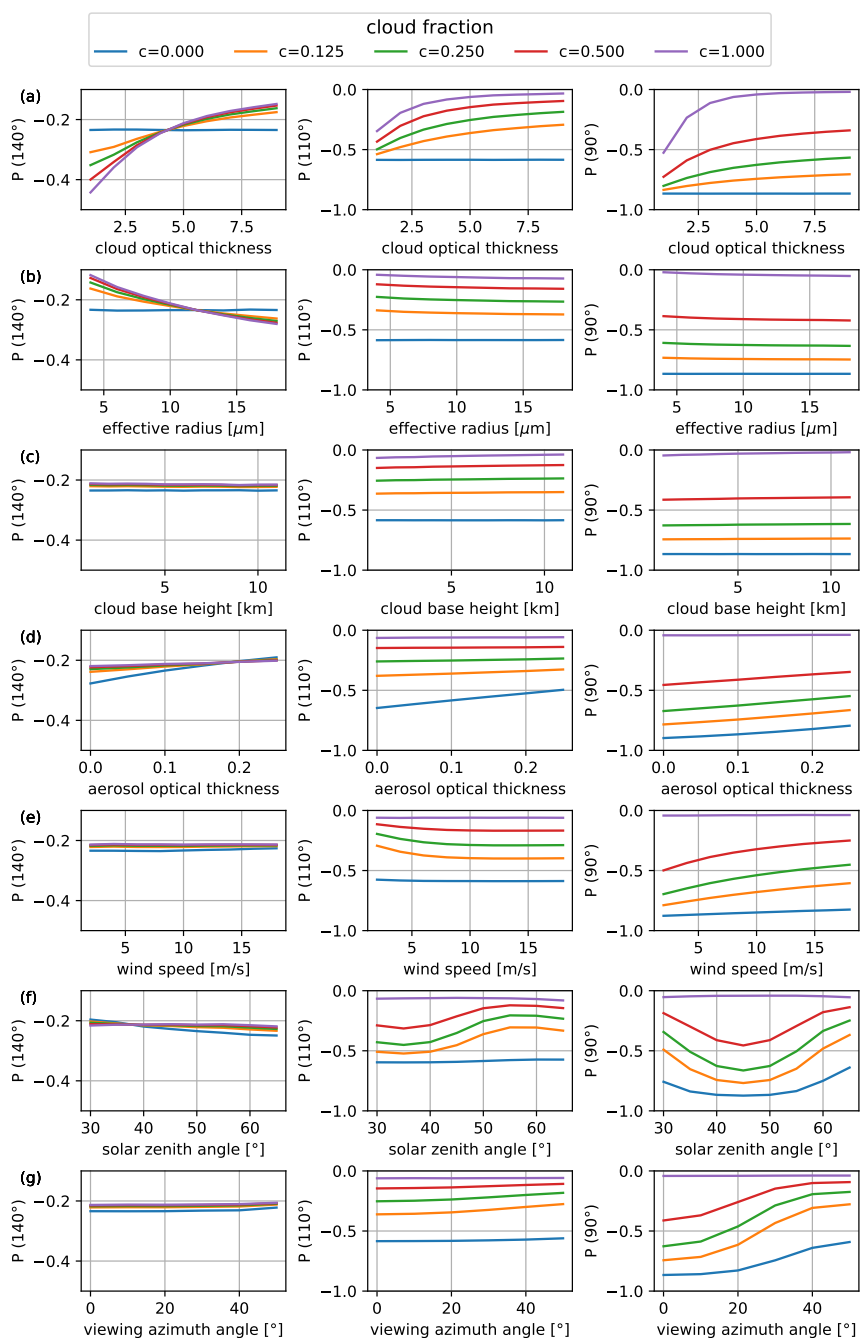
Figure 5. Dependencies of degree of polarization $P = Q/I$ at scattering angles of 140° (left), 110° (middle), and 90° (right) on cloud optical thickness, cloud droplet effective radius, cloud base height, aerosol optical thickness, wind speed, solar zenith angle, and viewing azimuth angle. The colors correspond to cloud fractions between 0 and 1 (see legend).

To assess the robustness of the retrieval method we performed additional sensitivity studies which are presented in Fig. 5.

190   The base case for all simulations is defined as follows: ocean surface, cloud layer at 2-3 km altitude with an optical thickness of τ_c=5, cloud droplet effective radius 10 μm, wind speed 5 m/s, aerosol optical thickness τ_a=0.1, solar zenith angle 50°. Starting from the base case, one of the parameters is varied whereas all other parameters are kept constant. We also include results for a scattering angle of 110°, not in the maximum of the sun-glint. The panels in the left column of Fig. 5 show the sensitivities for $P(140°)$, the middle ones correspond to $P(110°)$, and those in the right column are for $P(90°)$.

195   In scenario (a) the cloud optical thickness τ_c is varied: as shown before $|P(140°)|$ decreases with increasing τ_c for all cloud fractions c. For $\tau_c \lesssim 4$, the lines corresponding to different cloud fractions separate whereas for larger τ_c, $P(140°)$ is almost independent of cloud fraction. For $P(110°)$ and $P(90°)$ the lines corresponding to different cloud fractions clearly separate. In scenario (b) the droplet effective radius is varied: Here $|P(140°)|$ increases with increasing effective radius. This implies that in order to retrieve an accurate optical thickness, the retrieval lookup table needs to be generated for the correct effective radius.

200   A way to realize this is to combine the retrieval with an effective radius retrieval based on the cloudbow signature. $P(110°)$ and $P(90°)$ are almost independent of effective radius, therefore the cloud fraction retrieval does not require prior information on droplet size. In scenario (c) the cloud base height is varied, whereas the geometrical thickness of the cloud is kept constant as 1 km. $P(140°)$, $P(110°)$, and $P(90°)$ are almost independent of cloud height. This is a favorable outcome, suggesting that the retrieval process does not need prior information regarding cloud height. In scenario (d) the aerosol optical thickness is varied:

205    $P(140°)$ remains constant, while $P(110°)$ and $|P(90°)|$ slightly decrease with increasing aerosol optical thickness τ_a. These findings indicate that having prior information on τ_a would enhance the accuracy of the cloud fraction retrieval. In scenario (e) the wind speed is varied: $P(140°)$ is not impacted by the sun-glint, therefore it is independent of wind speed. $P(90°)$ is independent of wind speed for clear sky pixels and for fully cloudy pixels but not for partially cloudy pixels. Therefore, prior information about wind speed from independent observations should be taken into account. $P(110°)$, at a scattering angle not

210   in the center of the sun-glint, depends much less on the wind speed. This shows, that if there is no prior knowledge of wind speed, it may be better to use $P(110°)$ instead of $P(90°)$ although the polarization signal is weaker. In scenario (f) the solar zenith angle is varied: Again $P(140°)$ is constant but $P(90°)$ and $P(110°)$ vary, because the position of the glint depends on the solar zenith angle. The maximum of the glint is always at the mirror reflection angle, i.e., it moves towards larger scattering angle as the solar zenith angle increases. For a solar zenith angle of 45° the maximum of the sun-glint is at 90° scattering angle.

215   In scenario (g) the viewing azimuth angle is varied, which does not have an impact on $P(140°)$. For $P(90°)$ the impact is quite large, because as the viewing azimuth angle changes, the observing direction moves away from the center of the sun-glint. For $P(110°)$ this dependence is much weaker, as the viewing direction is not close the the center of the sun-glint.

In summary, the simulations suggest that the retrieval method is expected to deliver accurate cloud fractions and cloud optical thicknesses over the ocean, provided there is approximate prior information about wind speed and effective radius.

3 Test with high spatial resolution aircraft data

In this section we test the retrieval method using airborne observations taken by the specMACS instrument on the HALO aircraft during the EUREC4A measurement campaign.

3.1 Polarimetric observations with specMACS polarization cameras

The spectrometer of the Munich Aerosol Cloud Scanner (specMACS; Ewald et al., 2016) consists of two hyperspectral line cameras covering the spectral range from 400 to 2500 nm and two identical polarization-sensitive imaging cameras (Pörtge et al., 2023; Weber et al., 2023). The two polarization-sensitive cameras have a combined maximum field of view of about $\pm 91° \times \pm 117°$ (along track × across track). This results in a horizontal resolution of 10–20 m at ground when the flight altitude is around 10 km. The cameras take images at an acquisition frequency of 8 Hz. The sensors include on-chip directional polarizing filters which allow to measure the intensity and the linear polarization, i.e. the Stokes vector components I, Q, and U. These are geometrically and radiometrically calibrated (Weber et al., 2023). The central wavelengths (bandwidth) of specMACS are approximately 621 nm (66 nm), 547 nm (117 nm) and 468 nm (82 nm). In the following we use data that were measured during the EUREC4A (ElUcidating the RolE of Cloud-Circulation Coupling in ClimAte) field campaign which took place in January and February 2020 with base in Barbados (Stevens et al., 2021). All observations during the EUREC4A campaign were taken over ocean.

We selected six scenes including shallow cumulus clouds observed on 28th of January 2020. These contain various cloud fractions, from almost clear to almost fully cloud covered. The size of the scenes is approximately 2.5×2.5 km^2 corresponding to the pixel size of e.g. HARP2 and the spatial resolution of the data is approximately 10 m. The images corresponding to the selected scenes $s1$ to $s6$ are presented in Fig. 6, where each cloud scene is shown at scattering angles around 110° (left) and at scattering angles around 140° (right). Note that in the left images the ocean surface is clearly brighter than in the right images due to the sun-glint whereas the brightness of the clouds is similar in both images. Across an image the scattering angle is not constant. Since we require observations at particular scattering angles we use the geo-localization of cloud targets as described in Kölling et al. (2019) and Pörtge et al. (2023) in order to obtain all pixels in the chosen region for a given scattering angle. Pixels obtained using this method are averaged to get the Stokes vector of a selected scene for a given scattering angle. Combining all scattering angles results in the phase curves for the selected scenes which shown in Fig. 7 for the red channel of specMACS centered at 620 nm. Since the observations are not taken exactly in the solar principal plane, the U-component of the Stokes vector becomes non-zero and we calculate the degree of polarization as follows:

$$P = -\frac{\sqrt{Q^2 + U^2}}{I} \tag{8}$$

The negative sign indicates that the radiation is predominantly polarized in the direction perpendicular to the scattering plane, i.e. P has the same sign as Q/I in the solar principal plane so that the curves can be compared to the simulations shown in Section 2.2. As expected we find that $|P|$ decreases with increasing cloud amount in the scenes ($s1$ is the scene including very few clouds and $s5$ and $s6$ are almost fully cloud covered).
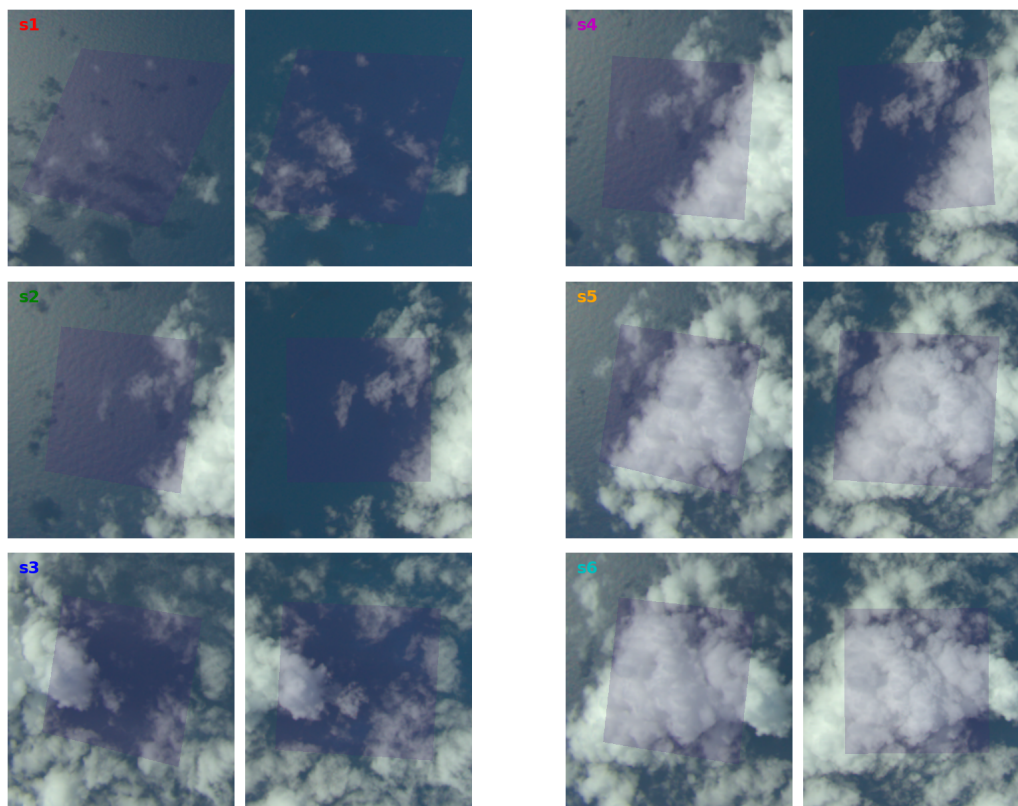
Figure 6. Six selected cloud scenes s1–s6 observed by specMACS over ocean. The size of the shaded area in each image is approximately $2.5 \times 2.5 \ \mathrm{km}^2$. For each of the scenes the cloud field is observed from different viewing directions during the overflight. In the left images of each scene, the average scattering angle over the shaded region is 110° and in the right images it is 140°.
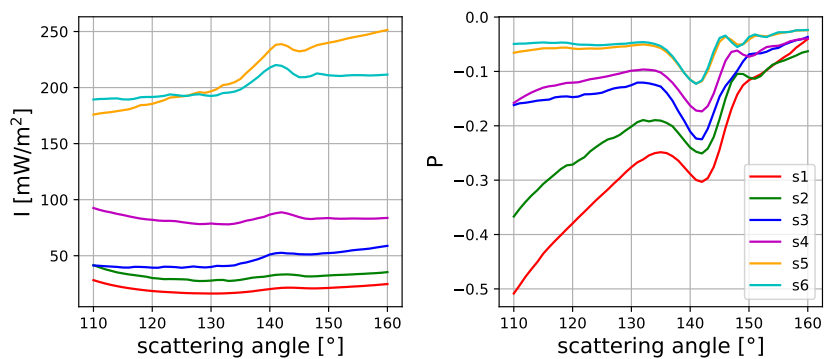
Figure 7. Phase curves of I and P observed by specMACS in the red channel centered at 620 nm for the selected scenes which are shown in the images of Fig. 6.

In order to retrieve cloud fraction and cloud optical thickness from specMACS data we generate a lookup table for the specific time and conditions when the observations were taken. We performed monochromatic simulations for the center wavelength of the red channel (621nm). The solar zenith angle was 46.5° and we know that the aerosol optical thickness on the particular day

255   was about 0.08 (Chazette et al., 2022). For simplicity we use a typical wind speed of 5 m/s, which is in agreement with Special Sensor Microwave Imager Sounder (SSMIS) observations (Wentz et al., 2012). We also applied standard values for the water cloud droplet size distribution: an effective radius of 10 μm and an effective variance of 0.1. Results of the cloudbow retrieval show that these values are realistic (compare Table 1). As we have demonstrated in the sensitivity analysis in Section 2.2.3, inaccurate assumptions on cloud-size distribution parameters produce errors in the retrieval of cloud optical thickness while the

260   cloud cover retrieval is not affected. With specMACS we can not obtain scattering angles of 140° and 90° for the same cloud scene, therefore we use 140° and 110° to generate the lookup table shown in Fig. 8. The colored dots plotted on top of the
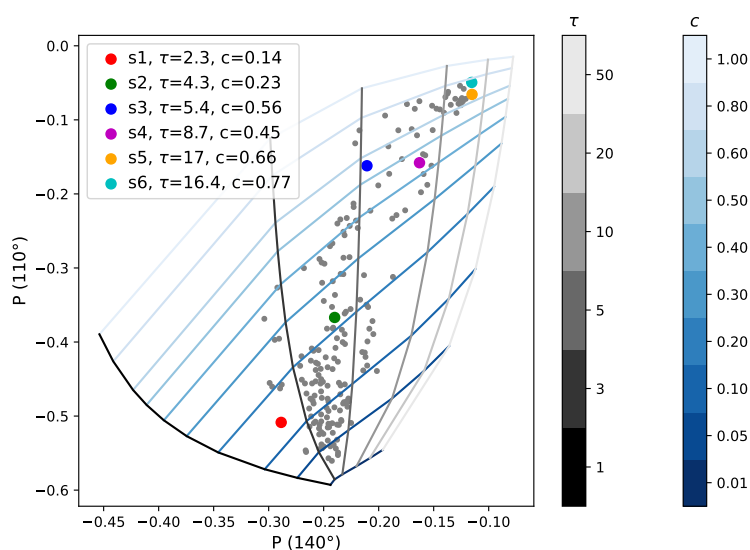
Figure 8. Retrieval lookup table and observational data. The colored dots represent the observed values of the selected scenes shown in Fig. 6. The legend includes the retrieved optical thickness and cloud fraction values for those points. The grey dots are all data points gathered during one research flight on 28th January 2020 (observations averaged to 2.5 km spatial resolution).

lookup table correspond to the observational data of the selected scenes. Using a bi-linear interpolation between the simulated grid points of the lookup table we retrieve the values for cloud optical thickness τ and cloud fraction c as included in the legend of Fig. 8. We also employed the cloud fraction retrieval method outlined in (Pörtge et al., 2023) on the images of the selected

265   scenes. The method is based on intensity thresholds and color ratios. Results for the selected scenes are included in Table 1). For scene $s1$ we obtain τ=2.3 and c=0.14 from the lookup-table. The threshold based retrieval algorithm in this case yields a higher cloud fraction of c=0.37. Comparing to the images in Fig. 6 the smaller cloud fraction seems more realistic. For scene $s2$ the lookup table yields τ=4.3 and c=0.23 which for this scene corresponds well to the threshold based retrieved value of c=0.20 and which looks reasonable when compared to the images. Scene $s4$ includes partly the same clouds as scene $s2$ but in

retrieval method	lookup-table		threshold	cloudbow	
scene	τ	c	c	r_{eff}	v_{eff}
s1	2.3	0.14	0.37	7.4	0.28
s2	4.3	0.23	0.20	9.5	0.09
s3	5.4	0.56	0.54	9.6	0.31
s4	8.7	0.45	0.45	10.6	0.09
s5	17.0	0.66	0.99	13.8	0.08
s6	16.4	0.77	0.96	14.9	0.05

Table 1. Cloud fraction retrieval results from lookup table method and from threshold method for selected scenes.

addition a larger part of the thicker cloud as seen in the lower right part of the images. Consistently, we get for scene $s4$ larger values for optical thickness (τ=8.7) and cloud cover (c=0.45), corresponding perfectly to threshold based retrieval with c=0.45. In scene $s3$ the images show a clear area in the center surrounded by clouds from all directions. Although in the RGB image the sun-glint is not well visible, the lookup table based retrieval yields reasonable results of τ=5.4 and c=0.56. Again the cloud fraction corresponds very well to the threshold based retrieval with c=0.54. The last two scenes $s5$ and $s6$ include the same clouds which are slightly shifted from one scene to the next. The upper left part of scene $s5$ is cloud free whereas scene $s6$ is almost completely filled with clouds with some small gaps. The retrieved τ is therefore very similar in both scenes (τ=17.0 for $s5$ and τ=16.4 for $s6$) whereas the cloud fraction is significantly larger for $s6$ as expected by looking at the images (c=0.66 for $s5$ and c=0.77 for $s6$). For these two cases the threshold based algorithm yields higher cloud fraction values (c=0.99 for $s5$ and c=0.96 for $s6$), it seems that the algorithm does not detect the small gaps between thicker clouds as cloud-free.

The gray dots included in the lookup table in Fig. 8 correspond to all observations taken during a one hour period of the research flight on 28th of January 2020, for which the viewing azimuth angle is not more than 40° away from the principal plane making sure that the sun-glint is contained. In this range, $P(110°)$ does not depend much on viewing azimuth angle (compare Fig. 5). All dots are within the lookup table grid which means that the retrieval yields values for each observation. The retrieved cloud fractions and optical thicknesses are shown as histograms in Fig. 9. The EUREC4A campaign focused on shallow cumulus clouds which were also observed on 28th of January 2020. The optical thickness of this type of clouds is usually quite small which can also be seen in the cloud optical thickness histogram that we obtain for the particular flight, showing an optical thickness below 10 for the majority of the points. The horizontal extent of the clouds can be several kilometers, therefore a large range of cloud fraction values between 0 and 0.8 is covered by the observations. The majority of points has relatively low cloud fractions smaller than 0.2. In Fig. 10, the retrieved cloud fractions obtained through the lookup-table method are plotted on the x-axis versus the retrieved cloud fractions obtained through the threshold method on the y-axis. The linear regression line has a slope of 0.95, and the correlation coefficient is 0.88. Specifically, within the high cloud fraction regime, the scatter plot demonstrates that the threshold-based retrieval results in larger cloud fractions compared to the lookup table-based retrieval, a pattern consistently observed in the selected scenes $s5$ and $s6$. The strong correlation underscores that
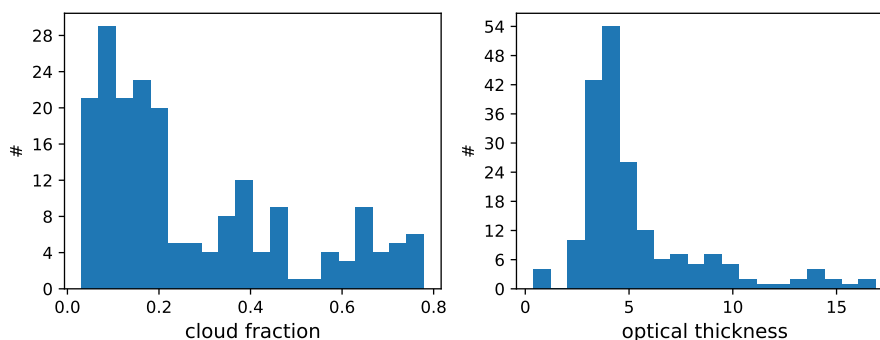
Figure 9. Histogram of retrieved cloud fractions and optical thicknesses using the lookup table method.
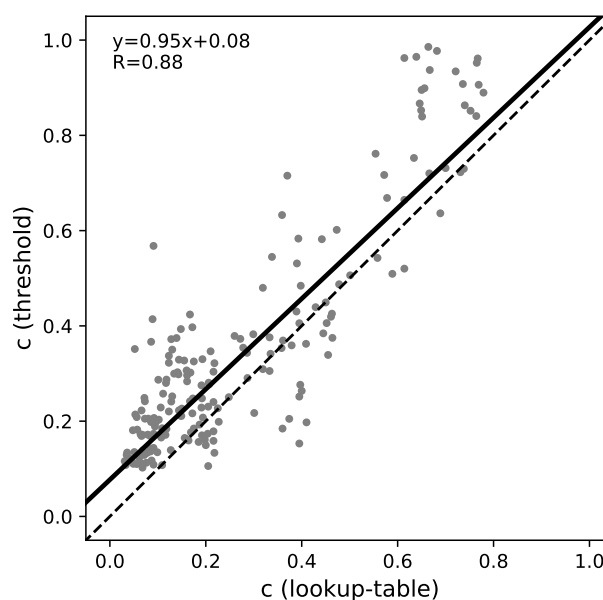
Figure 10. Cloud fractions derived by the lookup table method versus cloud fractions derived using a combined threshold and color ratio method.

the straightforward and robust lookup table retrieval method provides reasonable cloud fraction values for the entire flight's
295 observations.

4 Conclusions and Outlook

We have presented an innovative and straightforward approach to retrieve cloud fraction and optical thickness from multi-angle
polarization observations over ocean. This retrieval method could be a valuable addition for instance to the cloud retrieval chain

for the PACE mission including the polarimeters HARP2 and SPEXone. Given the typical spatial resolution of upcoming
300 polarized satellite-based measurements of approximately 2-3 km, this technique becomes particularly valuable for acquiring
sub-pixel information about clouds.

The fundamental principle of this method lies in the distinctive angular polarization patterns generated by the interaction of
radiation with various components of the Earth's atmosphere-surface system. Specifically, cloud scattering generates polariza-
tion at cloudbow scattering angles, while ocean surface reflection results in the strongly polarized sun-lint around the mirror
305 reflection angle. Consequently, by analyzing the angular polarization pattern, we can effectively separate the contributions of
clouds and the surface to the observed polarized intensity.

Our sensitivity study reveals that the complete angular pattern of polarized intensity is not required. Instead, two specific
scattering angles – one within the cloudbow and one within the sun-glint – are sufficient. Utilizing a 1D vector radiative transfer
code, we generated lookup tables that incorporate the simulated degree of polarization at 140° and 90° scattering angles for
310 various cloud optical thicknesses between 0 and 50. To calculate polarized intensities for partially cloudy pixels we employ
the independent pixel approximation. When we plot the degree of polarization at 140° scattering angle against the degree of
polarization at 90° scattering angle and connect data points of constant optical thickness and data points of constant cloud
cover, we obtain well-separated lines, forming an almost rectangular lookup table grid. We examined the influence of cloud
droplet size, cloud height, aerosol optical thickness, and wind speed on the retrieval accuracy. We found that the retrieval
315 results are almost independent of cloud height. The cloud fraction retrieval slightly depends on aerosol optical thickness and
on wind speed, therefore prior knowledge on these parameters is advantageous. The retrieval of cloud optical thickness depends
on droplet radius. Hence, deriving this parameter, for instance, through methods like the cloudbow retrieval, can significantly
enhance accuracy.

We tested the method using specMACS observations conducted aboard the HALO aircraft during the EUREC4A campaign,
320 focusing on shallow cumulus clouds over the ocean. Operating at a high spatial resolution of approximately 10-20 m, spec-
MACS data was averaged over domains of approximately 2.5×2.5 km^2 to emulate satellite observations. Subsequently, the
retrieval algorithm was applied to the resulting degree of polarization at scattering angles of 140° and 110°. The retrieved
optical thicknesses were typically below 10, a realistic range for the observed cloud type, and cloud fractions in the range be-
tween 0 and 0.8 were retrieved. We selected six scenes, representing low, medium, and high cloud fractions. We analyzed the
325 high-resolution images to visually verify the consistency between the retrieved cloud fraction and the images. For all selected
scenes, the retrieved cloud fractions matched the visual expectations. Additionally, we applied another cloud fraction retrieval
method based on intensity thresholds and color ratios (Pörtge et al., 2023). We find a good correlation between the results of
the two cloud fraction retrieval methods, providing further evidence of the performance of the straightforward lookup-table
retrieval approach.

330 In a subsequent study, we intend to further evaluate the accuracy of the retrieval algorithm using synthetic data. This data will
be generated using the 3D vector radiative transfer code MYSTIC. As we know the true optical thicknesses and cloud fractions
for the synthetic dataset, assessing the retrieval accuracy becomes straightforward by comparing the obtained results with the
model input. This approach will enable us to quantify the effects of 3D cloud scattering, including in-scattering and shadowing,

on the retrieval results. We have successfully applied this methodology to validate the accuracy the cloud microphysics retrieval
(Volkmer et al., 2023) and to investigate the impact of 3D cloud scattering on trace gas retrievals (Emde et al., 2022; Yu et al., 2022; Kylling et al., 2022).

Once the data from the PACE mission becomes accessible, we plan to employ our methodology on the satellite observations. The algorithm can be applied to both HARP2 and SPEXone data. We intend to test the cloud fraction retrieval by comparing the obtained results with images captured by the OCI instrument onboard PACE, which operates at a higher spatial resolution of 1.2×1.2 km^2. This comparative analysis will further verify the reliability of our cloud fraction retrieval.

Author contributions. CE performed the sensitivity studies, set up the retrieval method, performed the tests on specMACS observations, and wrote the manuscript. VP provided the specMACS data. MM and BM helped to set up and improve the retrieval methodology. All authors contributed to the interpretation of the results and helped to improve the manuscript.

Competing interests. The contact author has declared that none of the authors has any competing interests.

References

Alexandrov, M. D., Cairns, B., Emde, C., Ackerman, A. S., and van Diedenhoven, B.: Accuracy assessments of cloud droplet size retrievals from polarized reflectance measurements by the research scanning polarimeter, Remote Sensing of Environment, 125, 92 – 111, 2012.

Anderson, G., Clough, S., Kneizys, F., Chetwynd, J., and Shettle, E.: AFGL atmospheric constituent profiles (0-120 km), *Tech. Rep. AFGL-TR-86-0110*, Air Force Geophys. Lab., Hanscom Air Force Base, Bedford, Mass., 1986.

Bréon, F.-M. and Doutriaux-Boucher, M.: A comparison of Cloud Droplet Radii Measured from Space, IEEE Transactions on Geoscience and Remote Sensing, 43, 1769–1805, 2005.

Buras, R. and Mayer, B.: Efficient unbiased variance reduction techniques for Monte Carlo simulations of radiative transfer in cloudy atmospheres: The solution, J. Quant. Spectrosc. Radiat. Transfer, 112, 434–447, 2011.

Chandrasekhar, S.: Radiative Transfer, Oxford Univ. Press, UK, 1950.

Chazette, P., Baron, A., and Flamant, C.: Mesoscale spatio-temporal variability of airborne lidar-derived aerosol properties in the Barbados region during EUREC^{4}A, Atmospheric Chemistry and Physics, 22, 1271–1292, https://doi.org/10.5194/acp-22-1271-2022, 2022.

Cox, C. and Munk, W.: Measurement of the roughness of the sea surface from photographs of the sun's glitter, Journal of the Optical Society of America, 44, 838–850, 1954a.

Cox, C. and Munk, W.: Statistics of the sea surface derived from sun glitter, Journal of Marine Research, 13, 198–227, 1954b.

Emde, C., Buras, R., Mayer, B., and Blumthaler, M.: The impact of aerosols on polarized sky radiance: model development, validation, and applications, Atmos. Chem. Phys., 10, 383–396, 2010.

Emde, C., Barlakas, V., Cornet, C., Evans, F., Korkin, S., Ota, Y., Labonnote, L. C., Lyapustin, A., Macke, A., Mayer, B., and Wendisch, M.: IPRT polarized radiative transfer model intercomparison project - Phase A, J. Quant. Spectrosc. Radiat. Transfer, 164, 8–36, https://doi.org/10.1016/j.jqsrt.2015.05.007, 2015.

Emde, C., Buras-Schnell, R., Kylling, A., Mayer, B., Gasteiger, J., Hamann, U., Kylling, J., Richter, B., Pause, C., Dowling, T., and Bugliaro, L.: The libRadtran software package for radiative transfer calculations (version 2.0.1), Geophy. Mod. Dev., 9, 1647–1672, https://doi.org/10.5194/gmd-9-1647-2016, 2016.

Emde, C., Barlakas, V., Cornet, C., Evans, F., Wang, Z., Labonotte, L. C., Macke, A., Mayer, B., and Wendisch, M.: IPRT polarized radiative transfer model intercomparison project – Three-dimensional test cases (phase B), J. Quant. Spectrosc. Radiat. Transfer, 209, 19–44, https://doi.org/10.1016/j.jqsrt.2018.01.024, 2018.

Emde, C., Yu, H., Kylling, A., van Roozendael, M., Stebel, K., Veihelmann, B., and Mayer, B.: Impact of 3D cloud structures on the atmospheric trace gas products from UV–Vis sounders – Part 1: Synthetic dataset for validation of trace gas retrieval algorithms, Atmospheric Measurement Techniques, 15, 1587–1608, https://doi.org/10.5194/amt-15-1587-2022, 2022.

Ewald, F., Kölling, T., Baumgartner, A., Zinner, T., and Mayer, B.: Design and characterization of specMACS, a multipurpose hyperspectral cloud and sky imager, Atmospheric Measurement Techniques, 9, 2015–2042, https://doi.org/10.5194/amt-9-2015-2016, 2016.

Fougnie, B., Marbach, T., Lacan, A., Lang, R., Schlüssel, P., Poli, G., Munro, R., and Couto, A. B.: The multi-viewing multi-channel multi-polarisation imager – Overview of the 3MI polarimetric mission for aerosol and cloud characterization, Journal of Quantitative Spectroscopy and Radiative Transfer, 219, 23–32, https://doi.org/10.1016/j.jqsrt.2018.07.008, 2018.

Hansen, J. E. and Hovenier, J. W.: Interpretation of the Polarization of Venus, J. Atmos. Sci., 31, 1137 – 1160, https://doi.org/https://doi.org/10.1175/1520-0469(1974)031<1137:IOTPOV>2.0.CO;2, 1974.

Hansen, J. E. and Travis, L. D.: Light scattering in planetary atmospheres, Space Science Reviews, 16, 527–610, 1974.

Hasekamp, O. P.: Capability of multi-viewing-angle photo-polarimetric measurements for the simultaneous retrieval of aerosol and cloud properties, Atmospheric Measurement Techniques, 3, 839–851, https://doi.org/10.5194/amt-3-839-2010, 2010.

385 Hess, M., Koepke, P., and Schult, I.: Optical Properties of Aerosols and Clouds: The Software Package OPAC, Bulletin of the American Meteorological Society, 79, 831–844, 1998.

Intergovernmental Panel On Climate Change: Technical Summary, in: Climate Change 2013 – The Physical Science Basis, pp. 31–116, Cambridge University Press, 1 edn., https://doi.org/10.1017/CBO9781107415324.005, 2014.

Intergovernmental Panel On Climate Change: Climate Change 2021 – The Physical Science Basis: Working Group I Contribu-

390 tion to the Sixth Assessment Report of the Intergovernmental Panel on Climate Change, Cambridge University Press, 1 edn., https://doi.org/10.1017/9781009157896, 2023.

Kölling, T., Zinner, T., and Mayer, B.: Aircraft-based stereographic reconstruction of 3-D cloud geometry, Atmospheric Measurement Techniques, 12, 1155–1166, https://doi.org/10.5194/amt-12-1155-2019, 2019.

Kurucz, R. and Bell, B.: CD Rom No. 23, Smithonian Astrophys. Obs., extraterrestrial solar spectrum from 200–200000 nm, 1995.

395 Kylling, A., Emde, C., Yu, H., van Roozendael, M., Stebel, K., Veihelmann, B., and Mayer, B.: Impact of 3D cloud structures on the atmospheric trace gas products from UV–Vis sounders – Part 3: Bias estimate using synthetic and observational data, Atmospheric Measurement Techniques, 15, 3481–3495, https://doi.org/10.5194/amt-15-3481-2022, 2022.

Maignan, F., Bréon, F.-M., Fédèle, E., and Bouvier, M.: Polarized reflectances of natural surfaces: Spaceborne measurements and analytical modeling, Remote Sensing of Environment, 113, 2642–2650, https://doi.org/10.1016/j.rse.2009.07.022, 2009.

400 Mayer, B.: Radiative transfer in the cloudy atmosphere, European Physical Journal Conferences, 1, 75–99, 2009.

Mayer, B. and Kylling, A.: Technical note: The libRadtran software package for radiative transfer calclations – description and examples of use, Atmos. Chem. Phys., 5, 1855–1877, 2005.

Mie, G.: Beiträge zur Optik trüber Medien, speziell kolloidaler Metallösungen, Annalen der Physik, 330, 377–445, https://doi.org/10.1002/andp.19083300302, 1908.

405 Mishchenko, M. I. and Travis, L. D.: Satellite retrieval of aerosol properties over the ocean using polarization as well as intensity of reflected sunlight, J. Geophys. Res., 102, 16 989–17 013, 1997.

Nakajima, T. and King, M. D.: Determination of the optical thickness and effective particle radius of clouds from reflected solar radiation measurements. Part I: theory, Journal of the Atmospheric Sciences, 47, 1878–1893, 1990.

Platnick, S., Meyer, K. G., King, M. D., Wind, G., Amarasinghe, N., Marchant, B., Arnold, G. T., Zhang, Z., Hubanks, P. A., Holz, R. E.,

410 Yang, P., Ridgway, W. L., and Riedi, J.: The MODIS Cloud Optical and Microphysical Products: Collection 6 Updates and Examples From Terra and Aqua, IEEE Transactions on Geoscience and Remote Sensing, 55, 502–525, https://doi.org/10.1109/TGRS.2016.2610522, 2017.

Pörtge, V., Kölling, T., Weber, A., Volkmer, L., Emde, C., Zinner, T., Forster, L., and Mayer, B.: High-spatial-resolution retrieval of cloud droplet size distribution from polarized observations of the cloudbow, Atmospheric Measurement Techniques, 16, 645–667, https://doi.org/10.5194/amt-16-645-2023, 2023.

415 Remer, L. A., Knobelspiesse, K., Zhai, P.-W., Xu, F., Kalashnikova, O. V., Chowdhary, J., Hasekamp, O., Dubovik, O., Wu, L., Ahmad, Z., Boss, E., Cairns, B., Coddington, O., Davis, A. B., Dierssen, H. M., Diner, D. J., Franz, B., Frouin, R., Gao, B.-C., Ibrahim, A., Levy, R. C., Martins, J. V., Omar, A. H., and Torres, O.: Retrieving Aerosol Characteristics From the PACE Mission, Part 2: Multi-Angle and Polarimetry, Frontiers in Environmental Science, 7, https://doi.org/10.3389/fenvs.2019.00094, 2019.

Stap, F., Hasekamp, O., Emde, C., and Röckmann, T.: Influence of 3D effects on 1D aerosol retrievals in synthetic, partially clouded scenes,

420 J. Quant. Spectrosc. Radiat. Transfer, 170, 54 – 68, https://doi.org/http://dx.doi.org/10.1016/j.jqsrt.2015.10.008, 2016a.

Stap, F. A., Hasekamp, O. P., Emde, C., and Rockmann, T.: Multiangle photopolarimetric aerosol retrievals in the vicinity of clouds: Synthetic study based on a large eddy simulation, J. Geophys. Res., 121, 12 914–12 935, https://doi.org/10.1002/2016JD024787, 2016b.

Sterzik, M. F., Bagnulo, S., Emde, C., and Manev, M.: The cloudbow of planet Earth observed in polarisation, Astron. Astrophys., 639, A89, https://doi.org/10.1051/0004-6361/202038270, 2020.

425 Stevens, B., Bony, S., Farrell, D., Ament, F., Blyth, A., Fairall, C., Karstensen, J., Quinn, P. K., Speich, S., Acquistapace, C., Aemisegger, F., Albright, A. L., Bellenger, H., Bodenschatz, E., Caesar, K.-A., Chewitt-Lucas, R., de Boer, G., Delanoë, J., Denby, L., Ewald, F., Fildier, B., Forde, M., George, G., Gross, S., Hagen, M., Hausold, A., Heywood, K. J., Hirsch, L., Jacob, M., Jansen, F., Kinne, S., Klocke, D., Kölling, T., Konow, H., Lothon, M., Mohr, W., Naumann, A. K., Nuijens, L., Olivier, L., Pincus, R., Pöhlker, M., Reverdin, G., Roberts, G., Schnitt, S., Schulz, H., Siebesma, A. P., Stephan, C. C., Sullivan, P., Touzé-Peiffer, L., Vial, J., Vogel, R., Zuidema, P., Alexander,
430 N., Alves, L., Arixi, S., Asmath, H., Bagheri, G., Baier, K., Bailey, A., Baranowski, D., Baron, A., Barrau, S., Barrett, P. A., Batier, F., Behrendt, A., Bendinger, A., Beucher, F., Bigorre, S., Blades, E., Blossey, P., Bock, O., Böing, S., Bosser, P., Bourras, D., Bouruet-Aubertot, P., Bower, K., Branellec, P., Branger, H., Brennek, M., Brewer, A., Brilouet, P.-E., Brügmann, B., Buehler, S. A., Burke, E., Burton, R., Calmer, R., Canonici, J.-C., Carton, X., Cato Jr., G., Charles, J. A., Chazette, P., Chen, Y., Chilinski, M. T., Choularton, T., Chuang, P., Clarke, S., Coe, H., Cornet, C., Coutris, P., Couvreux, F., Crewell, S., Cronin, T., Cui, Z., Cuypers, Y., Daley, A., Damerell,
435 G. M., Dauhut, T., Deneke, H., Desbios, J.-P., Dörner, S., Donner, S., Douet, V., Drushka, K., Dütsch, M., Ehrlich, A., Emanuel, K., Emmanouilidis, A., Etienne, J.-C., Etienne-Leblanc, S., Faure, G., Feingold, G., Ferrero, L., Fix, A., Flamant, C., Flatau, P. J., Foltz, G. R., Forster, L., Furtuna, I., Gadian, A., Galewsky, J., Gallagher, M., Gallimore, P., Gaston, C., Gentemann, C., Geyskens, N., Giez, A., Gollop, J., Gouirand, I., Gourbeyre, C., de Graaf, D., de Groot, G. E., Grosz, R., Güttler, J., Gutleben, M., Hall, K., Harris, G., Helfer, K. C., Henze, D., Herbert, C., Holanda, B., Ibanez-Landeta, A., Intrieri, J., Iyer, S., Julien, F., Kalesse, H., Kazil, J., Kellman, A., Kidane,
440 A. T., Kirchner, U., Klingebiel, M., Körner, M., Kremper, L. A., Kretzschmar, J., Krüger, O., Kumala, W., Kurz, A., L'Hégaret, P., Labaste, M., Lachlan-Cope, T., Laing, A., Landschützer, P., Lang, T., Lange, D., Lange, I., Laplace, C., Lavik, G., Laxenaire, R., Le Bihan, C., Leandro, M., Lefevre, N., Lena, M., Lenschow, D., Li, Q., Lloyd, G., Los, S., Losi, N., Lovell, O., Luneau, C., Makuch, P., Malinowski, S., Manta, G., Marinou, E., Marsden, N., Masson, S., Maury, N., Mayer, B., Mayers-Als, M., Mazel, C., McGeary, W., McWilliams, J. C., Mech, M., Mehlmann, M., Meroni, A. N., Mieslinger, T., Minikin, A., Minnett, P., Möller, G., Morfa Avalos, Y., Muller, C., Musat, I.,
445 Napoli, A., Neuberger, A., Noisel, C., Noone, D., Nordsiek, F., Nowak, J. L., Oswald, L., Parker, D. J., Peck, C., Person, R., Philippi, M., Plueddemann, A., Pöhlker, C., Pörtge, V., Pöschl, U., Pologne, L., Posyniak, M., Prange, M., Quiñones Meléndez, E., Radtke, J., Ramage, K., Reimann, J., Renault, L., Reus, K., Reyes, A., Ribbe, J., Ringel, M., Ritschel, M., Rocha, C. B., Rochetin, N., Röttenbacher, J., Rollo, C., Royer, H., Sadoulet, P., Saffin, L., Sandiford, S., Sandu, I., Schäfer, M., Schemann, V., Schirmacher, I., Schlenczek, O., Schmidt, J., Schröder, M., Schwarzenboeck, A., Sealy, A., Senff, C. J., Serikov, I., Shohan, S., Siddle, E., Smirnov, A., Späth, F., Spooner, B., Stolla,
450 M. K., Szkółka, W., de Szoeke, S. P., Tarot, S., Tetoni, E., Thompson, E., Thomson, J., Tomassini, L., Totems, J., Ubele, A. A., Villiger, L., von Arx, J., Wagner, T., Walther, A., Webber, B., Wendisch, M., Whitehall, S., Wiltshire, A., Wing, A. A., Wirth, M., Wiskandt, J., Wolf, K., Worbes, L., Wright, E., Wulfmeyer, V., Young, S., Zhang, C., Zhang, D., Ziemen, F., Zinner, T., and Zöger, M.: EUREC[4]A, Earth System Science Data, 13, 4067–4119, https://doi.org/10.5194/essd-13-4067-2021, 2021.

Tsang, L., Kong, J. A., and Shin, R. T.: Theory of Microwave Remote Sensing, John Wiley, New York, 1985.

455 Van Diedenhoven, B., Hasekamp, O. P., and Landgraf, J.: Retrieval of cloud parameters from satellite-based reflectance measurements in the ultraviolet and the oxygen A-band, Journal of Geophysical Research: Atmospheres, 112, 2006JD008 155, https://doi.org/10.1029/2006JD008155, 2007.

Volkmer, L., Pörtge, V., Jakub, F., and Mayer, B.: Model-based evaluation of cloud geometry and droplet size retrievals from 2-D polarized measurements of specMACS, EGUsphere, 2023, 1–22, https://doi.org/10.5194/egusphere-2023-2235, 2023.

460   Weber, A., Kölling, T., Pörtge, V., Baumgartner, A., Rammeloo, C., Zinner, T., and Mayer, B.: Polarization upgrade of specMACS: calibration and characterization of the 2D RGB polarization resolving cameras, EGUsphere, pp. 1–29, https://doi.org/10.5194/egusphere-2023-2209, 2023.

Wentz, F. J., Hilburn, K., and Smith, D. K.: RSS SSMIS OCEAN PRODUCT GRIDS DAILY FROM DMSP F17 NETCDF V7, Dataset available online from the NASA Global Hydrometeorology Resource Center DAAC, Huntsville, Alabama, U.S.A.,

465   https://doi.org/http://dx.doi.org/10.5067/MEASURES/DMSP-F17/SSMIS/DATA301, 2012.

Wiscombe, W.: Improved Mie scattering algorithms, Appl. Opt., 19, 1505–1509, 1980.

Yu, H., Emde, C., Kylling, A., Veihelmann, B., Mayer, B., Stebel, K., and Van Roozendael, M.: Impact of 3D cloud structures on the atmospheric trace gas products from UV–Vis sounders – Part 2: Impact on NO_2 retrieval and mitigation strategies, Atmospheric Measurement Techniques, 15, 5743–5768, https://doi.org/10.5194/amt-15-5743-2022, 2022.